JSWSC

Topical Issue – Observing, modelling and forecasting TIDs and mitigating their impact on technology

RESEARCH ARTICLE   **OPEN ⌂ ACCESS**

Medium-scale traveling ionospheric disturbances created by primary gravity waves generated by a winter storm

Masaru Kogure[1,2,3,*] 🔵, Min-Yang Chou[2,3], Jia Yue[2,3], Yuichi Otsuka[4], Huixin Liu[1], Fabrizio Sassi[2] 🔵, Nicholas Pedatella[5] 🔵, Cora E. Randall[6], and V. Lynn Harvey[6]

[1] Department of Earth and Planetary Science, Kyushu University, Fukuoka, Japan
[2] NASA Goddard Space Flight Center, Greenbelt, MD, USA
[3] Physics Department, Catholic University of America, Washington, DC, USA
[4] Institute for Space-Earth Environmental Research, Nagoya University, Nagoya, Japan
[5] High Altitude Observatory, NSF National Center for Atmospheric Research, Boulder, CO, USA
[6] Laboratory for Atmospheric and Space Physics, University of Colorado, Boulder, CO, USA

Abstract – This study explores the meteorological source and vertical propagation of gravity waves (GWs) that drive daytime traveling ionospheric disturbances (TIDs), using the specified dynamics version of the SD-WACCM-X (Whole Atmosphere Community Climate Model with thermosphere-ionosphere eXtension) and the SAMI3 (Sami3 is Also a Model of the Ionosphere) simulations driven by SD-WACCM-X neutral wind and composition. A cold weather front moved over the northern-central USA (90–100°W, 35–45°N) during the daytime of 20 October 2020, with strong upward airflow. GWs with ~500–700 km horizontal wavelengths propagated southward and northward in the thermosphere over the north-central USA. Also, the perturbations were coherent from the surface to the thermosphere; therefore, the GWs were likely generated by vertical acceleration associated with the cold front over Minnesota and South Dakota. The convectively generated GWs had almost infinite vertical wavelength below ~100 km due to being evanescent. This implies that the GWs tunneled through their evanescent region in the middle atmosphere (where a squared vertical wavenumber is equal to or smaller than 0) and became freely propagating in the thermosphere and ionosphere. Medium-scale TIDs (MSTIDs) also propagated southward with the GWs, suggesting that the convectively generated GWs created MSTIDs.

Keywords: Gravity wave / Medium-scale traveling ionospheric disturbance / Traveling ionospheric disturbance modeling

1 Introduction

Traveling ionospheric disturbances (TIDs) are propagating plasma perturbations with wave-like structures in the ionosphere. Understanding and predicting the formation mechanisms of TIDs is critical for improving space weather forecasting systems (Zawdie et al., 2022) and the precision of the Global Navigation Satellite System (GNSS) applications (Hernández-Pajares et al., 2006, 2017).

TIDs are classified according to their temporal and spatial scales into two groups: large-scale (LSTIDs) and medium-scale (MSTIDs) (Hunsucker, 1982; Hocke & Schlegel, 1996; Otsuka, 2021). LSTIDs have horizontal wavelengths of longer than a thousand km and periods of 30 min to 3 h, while MSTIDs have horizontal wavelengths of several hundred kilometers and periods of 15 min to 1 h (Hunsucker, 1982).

There are two types of MSTIDs. The first type is induced by the Perkins instability. The occurrence of Perkins-type MSTIDs primarily peaks near the solstices (e.g., Lee et al., 2021), and propagates equatorward and westward only during nighttime (Kelley & Miller, 1997; Miller et al., 1997; Shiokawa et al., 2003; Martinis et al., 2011). The sporadic E instability or gravity waves (GWs) coupled with the Perkins instability are the primary mechanisms to explain the fast growth of electrified nighttime MSTIDs (e.g., Perkins, 1973; Yokoyama & Hysell, 2010; Chou et al., 2022, 2023). The second type of MSTID is induced by GWs, which can propagate in any direction during the daytime and nighttime (Hines, 1960; Hocke & Schlegel, 1996; Kelley & Miller, 1997; Miller et al., 1997; Kotake et al., 2007; Otsuka et al., 2013; Nicolls et al., 2014; Otsuka, 2021; Vadas & Azeem, 2021; Perwitasari et al., 2022; Themens et al., 2022; Zhang et al., 2022; Vadas et al., 2023). Unless they have

horizontal phase speeds much larger than the background wind speed, most GWs propagate approximately opposite to the direction of the horizontal wind which changes in time (Vadas, 2007; Fritts & Vadas, 2008). These latter MSTIDs propagate in the same direction as the GWs (Nicolls et al., 2014). Therefore, most of these latter MSTIDs propagate approximately opposite to the direction of the neutral horizontal wind. This propagation feature has been confirmed by observations (Crowley et al., 1987; Vadas & Crowley, 2010; Crowley & Rodrigues, 2012; Xu et al., 2024). GWs are vital to transporting momentum from the lower to the upper atmosphere, affecting the distribution of chemical constituents globally in the ionosphere and thermosphere (Hines, 1960; Hocke & Schlegel, 1996; Zawdie et al., 2022). Otsuka et al. (2013) reported that the latter type of MSTID tends to propagate equatorward during daytime. Otsuka et al. (2013) proposed this to be due to the maximum ion drag across the magnetic field lines; in other words, ion velocity perturbations parallel to the magnetic field lines are larger than perturbations perpendicular to the magnetic field lines (Otsuka et al., 2013; Nicolls et al., 2014; Huba et al., 2015). Therefore, the propagation direction of MSTIDs is affected by both ion drag and background wind.

Many observational and modeling studies provide clues that MSTIDs are generated by GWs originating in the lower atmosphere. These studies have shown that the potential sources of GWs that drive MSTIDs include earthquakes, volcanic eruptions, tropical cyclones, tsunamis, thunderstorms, and primary GW breaking (secondary GW generation) in the middle atmosphere (Hung & Kuo, 1978; Taylor & Hapgood, 1988; Vadas & Liu, 2009, 2013; Vadas & Crowley, 2010; Liu et al., 2011; Nishioka et al., 2013; Chou et al., 2016; Azeem et al., 2017; Miyoshi et al., 2018; Vadas & Azeem, 2021; Heale et al., 2022a, Takahashi et al., 2022; Wright et al., 2022; Yang et al, 2022; Vadas et al., 2023, 2022b). Vadas & Liu (2009, 2013) simulated primary and secondary GWs from deep convection and the induced TIDs using a local high-resolution deep convection model and the global Thermosphere-Ionosphere-Mesosphere-Electrodynamics General Circulation Model (TIME-GCM). The TIDs were generated from the secondary GWs at z~180 km from the dissipation of primary convectively generated GWs over Brazil and had horizontal wavelengths >2000 km due to the low model resolution of the TIME-GCM. Miyoshi et al. (2018) simulated TIDs generated by GWs in a global whole atmosphere-ionosphere coupled model, the Ground-to-topside model of Atmosphere and Ionosphere for Aeronomy (GAIA) with 1° × 1° horizontal resolution. The simulated TIDs were generated with 700–1500 km horizontal wavelengths and 45–90-min periods by neutral wind perturbations associated with upward propagating GWs. Those GWs were secondary waves emitted from altitudes of 80–100 km by breaking primary waves from the troposphere. Miyoshi et al. (2018) concluded that TIDs are associated with secondary GWs primarily originating from the upper mesosphere and lower thermosphere during boreal winter. However, their 1° × 1° spatial resolution could not fully resolve small-scale GWs or weather systems (convective wave sources). Recently, Vadas et al. (2023) simulated GWs from the Tonga eruption by using three models: the HIgh Altitude Mechanistic general Circulation Model (HIAMCM), Model for gravity wavE Source, Ray tracing and reconstruction (MESORAC), and SAMI3 (Sami3 is Also a Model of the Ionosphere) driven by HIAMCM.

The HIAMCM is a whole-atmosphere model for neutral dynamics with a ~150 km effective horizontal resolution, which is much higher than the GAIA used by Miyoshi et al. (2018). Vadas et al. (2023) showed that MSTIDs and LSTIDs created by the vertical updrafts generated by the Tonga volcanic eruption are induced by secondary GWs rather than by primary GWs and tunneling (leakage) of Lamb waves. Heale et al. (2022a) simulated primary and secondary GWs emitted from a thunderstorm squall-line using the 2D numerical Model for Acoustic-Gravity wave Interactions and Coupling (MAGIC), with 1-km horizontal resolution (Zettergren & Snively, 2015). They revealed that the primary GWs became more dominant than the secondary waves in the ionospheric F-region when the tropospheric source forcing strength became smaller. Their results demonstrated that the source activity in the troposphere significantly influences the spectra and propagation of thermospheric GWs, suggesting that numerical model resolution, which affects the reproducibility of weather systems, influences the simulation of TIDs.

To investigate the vertical coupling between a tropospheric weather system, GWs in the thermosphere, and MSTIDs driven by the GWs, we simulated the neutral atmosphere from the surface to the thermosphere and ionosphere from 15 to 30 October 2020 using SD-WACCM-X (Specified Dynamics Whole Atmosphere Community Climate Model with thermosphere-ionosphere eXtension) (Liu et al., 2018; Huba & Liu, 2020; Chou et al., 2023), with a horizontal resolution of ~0.5°. It should be noted that SD-WACCM-X is a hydrostatic model, unlike MAGIC, so our model cannot resolve acoustic gravity waves. This version of SD-WACCM-X has two times higher spatial resolution than the GAIA model used by Miyoshi et al. (2018). Thus, SD-WACCM-X can better resolve medium-scale weather systems and GW structures. Additionally, the thermospheric state from SD-WACCM-X is used to drive SAMI3 via one-way coupling (e.g., McDonald et al., 2015; Huba & Liu, 2020; Chou et al., 2023), hereafter referred to as SAMI3/SD-WACCM-X. This study focuses on a meteorological weather event (a strong upward airflow within an early season winter storm) whereby GWs were generated around a front on 20 October 2020, and subsequent MSTIDs appeared in the simulation of SAMI3 and propagated along with GWs across the central-to-eastern northern USA during daytime. This study aims to reveal the potential source and propagation process of GWs from the lower atmosphere into the thermosphere and ionosphere. This study shows how the convectively generated GWs trigger MSTIDs and discusses the GW generation mechanism associated with upward airflow and convection (i.e., vertical acceleration of air) within the early season winter storm. In Section 2, the whole atmosphere and ionosphere numerical models are described. Section 3 describes the weather conditions on 20 October 2020 and shows the simulated GWs and their propagation from their source to the thermosphere. Also, Section 3 shows MSTIDs caused by the GWs. Conclusions are provided in Section 4.

2 SD-WACCM-X and SAMI3/SD-WACCM-X

SD-WACCM-X (Sassi et al., 2013; Liu et al., 2018; Huba & Liu, 2020; Chou et al., 2023) and SAMI3/SD-WACCM-X (Huba & Krall, 2013; McDonald et al., 2015, 2018; Huba & Liu, 2020; Chou et al., 2023) are utilized in this study. These
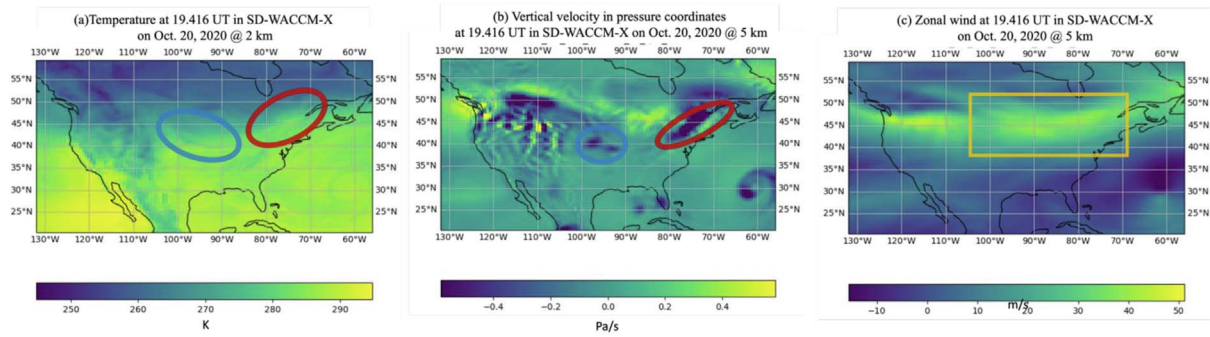
Figure 1. (a) Temperature over the USA at 2 km altitude at 19.416 UT on October 20, 2020 in SD-WACCM-X. (b) Vertical velocity in pressure coordinates (Pa/s) at 5 km altitude at 19.416 UT on October 20, 2020 in SD-WACCM-X. (c) Zonal wind at 5 km altitude at 19.416 UT on October 20, 2020 in SD-WACCM-X. The orange rectangle indicates the tropospheric jet. The blue and red ovals in panels (a) and (b) indicate the locations of cold and warm fronts, respectively.

simulations were also utilized by Chou et al. (2023). Here, the SD-WACCM-X meteorology is nudged to MERRA-2 (Modern-Era Retrospective analysis for Research and Applications version 2) up to ~50 km (see Smith et al., 2017). Above 50 km, SD-WACCM-X is free-running. The longitudinal and latitudinal resolutions of the neutral atmosphere and the ionosphere are $0.47° \times 0.625°$. The vertical resolution is less than 0.16 density scale height at pressures below 100 hPa and a quarter density scale height at pressures above 1 hPa (Pedatella et al., 2019). The resolution between 100 and 1 hPa decreases with altitude from 0.16 to 0.25 density scale heights. The temporal cadence of the model output is 5 min. Details of the ionosphere and thermosphere processes in WACCM-X (version 2) are described in Liu et al. (2018). The nudging process to the reanalysis in the troposphere and stratosphere is described in Smith et al. (2017).

SAMI3 is a global three-dimensional physics-based ionosphere model to simulate the plasma and chemical evolution of seven ion species (H^+, He^+, N^+, O^+, N_2^+, NO^+, and O_2^+) (Huba et al., 2017) between ~80 km and ~8 R_E. The neutral temperature, wind, and composition in SAMI3 can be specified from either empirical models or external numerical thermosphere models. In this study, the neutral variables from SD-WACCM-X are one-way coupled to drive the SAMI3 simulations (McDonald et al., 2015, 2018; Chou et al., 2023), referred to as SAMI3/SD-WACCM-X. The SAMI3 model was developed based on the SAMI2 model (Huba et al., 2000) by Huba et al. (2008). SAMI3 uses the Quasi-Dipole magnetic apex coordinate system. The geomagnetic latitude resolution is ~0.2° around the magnetic equator and 0.7° at 40° geomagnetic latitude at ~300 km. The geomagnetic longitude resolution is 4° except within the nested region of ~63.6–136.5°W (which includes the continental USA), where it is 0.6°. The temporal cadence of the SAMI3/SD-WACCM-X output is also 5 min.

This paper derives GW perturbations in the thermosphere in SD-WACCM-X with a temporal high-pass filter as follows. The neutral winds were averaged with a Gaussian weighting function over a 6-h moving window. The averaged value was then subtracted from the raw output data to eliminate its trend and low-frequency components (e.g., tides and their amplitude modulation), and then a Butterworth high-pass filter with a 2-h cutoff frequency was applied to the residuals for identifying the GWs with periods of 10 min to 2 h. This period range was determined based on TID observation studies (Boska & Sauli, 2001; Heale et al., 2020). To identify TIDs, the electron density in SAMI3/SD-WACCM-X was first interpolated to the grid of SD-WACCM-X, and then the aforementioned process was applied to the interpolated electron density. The residuals of electron density are defined as TIDs with 10 min to 2 h. The electron density shown in this paper is from SAMI3/SD-WACCM-X.

3 Simulation results

3.1 Weather conditions over the USA on 20 October 2020

We show the weather conditions over the continental USA on 20 October 2020 to investigate the potential source of the simulated GWs. Figure 1 shows (a) the temperature at ~2 km, (b) the vertical velocity in pressure coordinates at 5 km, and (c) the zonal wind at 5 km over the USA in the SD-WACCM-X simulation at 19.416 UT. Near the surface, the temperature difference between the southern and northern USA was ~30–40 K, and large temperature gradients exist over the northern Plains (40–50°N, 60–100°W) (Fig. 1a), indicating the presence of a weather front. The cold air advanced and displaced the warm air near ~40°N, 95°W (blue oval in Fig. 1a), forming a cold front. Since cold air lifts warm air in a front area, leading to mesoscale upward flow and convection, the negative vertical velocity in pressure coordinates (upward airflow) was enhanced (~6 $Pa \cdot s^{-1}$) on the warm air side (blue oval in Fig. 1b). This upward flow can generate GWs (Stull, 1976; Vadas & Fritts, 2009). Conversely, the positive vertical velocities (downward airflow) occur on the cold air side (~45–50°N, ~90–100°W), as expected, due to the cold air descending under the warm air. The warm air displaced the cold air near ~45°N, 75°W (red oval in Fig. 1a), forming a warm front, and the negative vertical velocity (upward airflow) was enhanced (>~6 $Pa \cdot s^{-1}$) on the warm side (red oval in Fig. 1b). These features of the large-scale weather system are consistent with the North American Mesoscale Forecast System (NAM) analysis* (Colbert et al., 2019). In addition, the National Weather Service reported an early winter storm with heavy rain and snow existed close to the cold front. This winter storm was captured by NEXRAD
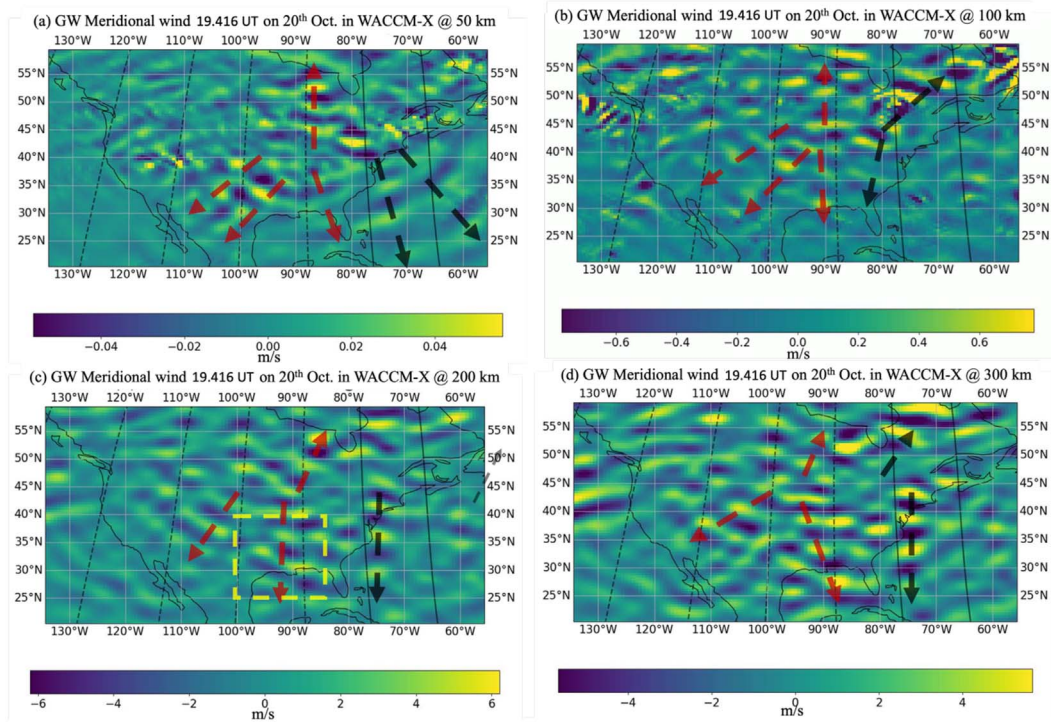
Figure 2. Gravity wave meridional wind perturbations (m·s^{-1}) at 50 km (a), 100 km (b), 200 km (c), and 300 km (d) altitudes at 19.416 UT on 20 October in SD-WACCM-X. Black and red arrows denote the propagation directions of GWs emitted from cold and warm fronts, respectively. GWs in the yellow rectangle in (c) will be discussed in detail later. See Movie 1 of the GW meridional winds at 16.33–22.33 UT for supporting information.

(NEXt generation weather RADar) (see Fig. S1c in the supporting information). Although convective activity in cold fronts is generally larger than in warm fronts, because of higher convective available potential energy, the upward flow in the SD-WACCM-X simulation was larger in the warm front than in the cold front. This larger upward flow is likely attributed to the Appalachian Mountains because a tropospheric jet (orange rectangle in Fig. 1c) flowed eastward over the Appalachian Mountains. Likewise, the upward airflow was also enhanced over ~50°N, 110–120°W, where the tropospheric jet flowed eastward over the Rocky Mountains. The two areas are known as hot spots of mountain waves (Hoffmann et al., 2013), making it challenging to distinguish convectively generated GWs from mountain waves. Therefore, those areas are excluded from the discussion.

3.2 GW generation mechanism and their propagation

This sub-section details the GWs emitted from the updraft along the front in SD-WACCM-X and their propagation from the lower atmosphere to the thermosphere. Figure 2 shows GW meridional wind perturbations at 50 km (a), 100 km (b), 200 km (c), and 300 km (d) in the SD-WACCM-X simulation on 20 October 2020, at 19.416 UT. GWs with ~500–700 km horizontal wavelengths propagated omnidirectionally over ~25–55°N, ~60–110°W at all the altitudes shown in Figure 2. These GWs propagated from the strong upward airflow within the cold front region (~40°N, 95°W) and within the warm front region (~45°N, 75°W) (see Movie 1 of the GW meridional

winds for 16.33–22.33 UT in supporting information), suggesting that the GWs at 200 and 300 km propagated from the lower atmosphere and their source could be the strong upward airflow within fronts shown in Section 3.1. These characteristics can also be seen in the zonal wind and temperature perturbations (not shown).

There are two potential physical generation mechanisms for the GWs. One of the generation mechanisms is spontaneous adjustment, which is a very well-known physical generation mechanism for front and jet GWs (Plougonven & Zhang, 2014). However, the spontaneous adjustment creates GWs with wavevectors parallel to the jet stream, whereas the wavevectors in SD-WACCM-X were omnidirectional. The second mechanism is the strong vertical upward airflow associated with fronts. Fronts can generate mesoscale upward airflow through baroclinic forcing, causing latent heat release (Stewart et al., 1995; Holton & Hakim, 2013). The latent heat can generate strong vertical upward airflow and convection. An upward (or downward) acceleration of air is a well-known mechanism for generating GWs, as shown by the theoretical solutions derived by Vadas & Fritts (2004) and Vadas (2013). These GWs have concentric structures, and the theoretical solutions were subsequently used to build a model for GWs generated by deep convective plumes (Vadas & Fritts, 2009; Vadas et al., 2009). Although deep convection has smaller horizontal scales than the strong vertical velocity associated with the cold front in SD-WACCM-X, the strong vertical airflow could create concentric GWs similar to deep convection, although with larger horizontal wavelengths. Also, a cumulus parameterization

scheme representing small-scale upward airflow, i.e., convection, can create concentric GWs (Kim et al., 2009). Liu et al. (2014) showed concentric GWs excited by parameterized deep convection in a tropical cyclone in WACCM, which is similar to the lower atmosphere part of the SD-WACCM-X simulation. We conclude, therefore, that the source of the simulated GWs is the strong upward airflow. This conclusion is consistent with observations of tropospheric concentric GWs generated by deep convection over the United States, as reported previously (e.g., Nishioka et al., 2013; Azeem et al., 2015). We also note, however, that concentric rings of GWs can be generated in the thermosphere from the body force, heating, and cooling created by the dissipation of primary GWs from deep convection (Vadas & Liu, 2009; Vadas, 2013).

Although apparent epicenters of the GWs at each altitude exist around the fronts, the correspondence of the phases among the altitudes is unclear in Figure 2. We investigate the vertical structure of the GW phase and their vertical wavelengths to reveal further the propagation process of the GWs from the troposphere to the thermosphere. Figure 3a shows the GW meridional wind perturbations as a function of latitude and altitude along 95°W (i.e., over the cold front) from the surface to 300 km at 19.416 UT (13.083 LT at 95°W). The phase lines for the northward propagating GWs south of ~40°N are coherent from the troposphere to the thermosphere, supporting our hypothesis that the thermosphere GWs shown in Figures 2c and 2d originated in the troposphere. Conversely, the phase structures north of ~40°N are complicated because of interference between northward and southward propagating GWs, so we decompose the GW perturbations into northward and southward Fourier components in Figures 3b and 3c. While the coherent phase lines for the southward propagating GWs in Figure 3b can be seen south of ~40°N as in Figure 3a, the phase lines for the northward GWs in Figure 3c are also coherent from the troposphere to the thermosphere. This result suggests that those GWs were emitted from 40 to 43°N, where the cold front and strong upward velocity appeared (see Fig. 3d) and propagated both southward and northward, displaying a cone shape. The coherent phase lines in Figure 3b can also be seen north of the cold front, propagating southward from a latitude higher than ~50°N and interfering with the convectively generated GWs propagating northward. Their sources are not likely the cold front over the continental USA but could exist in the troposphere in the North Polar Region (≥60°N). The GWs originating at high latitudes have 2–3 times smaller amplitudes than the convectively generated GWs, so this paper focuses on the convectively generated GWs.

Interestingly, the vertical wavelengths of the GWs were almost infinite below ~100 km altitude (i.e., the phases were nearly constant vertically), although the vertical wavelengths for the northward and southward propagating GWs above ~100 km altitude were ~110 km and ~150 km, respectively. These results suggest that the GWs were in an evanescent mode below ~100 km, tunneled from the surface to ~100 km, and changed to an internally propagating mode above ~100 km (Gavrilov & Kshevetskii, 2018; Heale et al., 2022a; Nappo, 2013; Walterscheid & Hecht, 2003). To investigate the GW propagation further, the local GW intrinsic horizontal phase speed and vertical wavelength, m, are calculated using the following local dispersion relation equation from equation (1b) in Marks & Eckermann (1995):
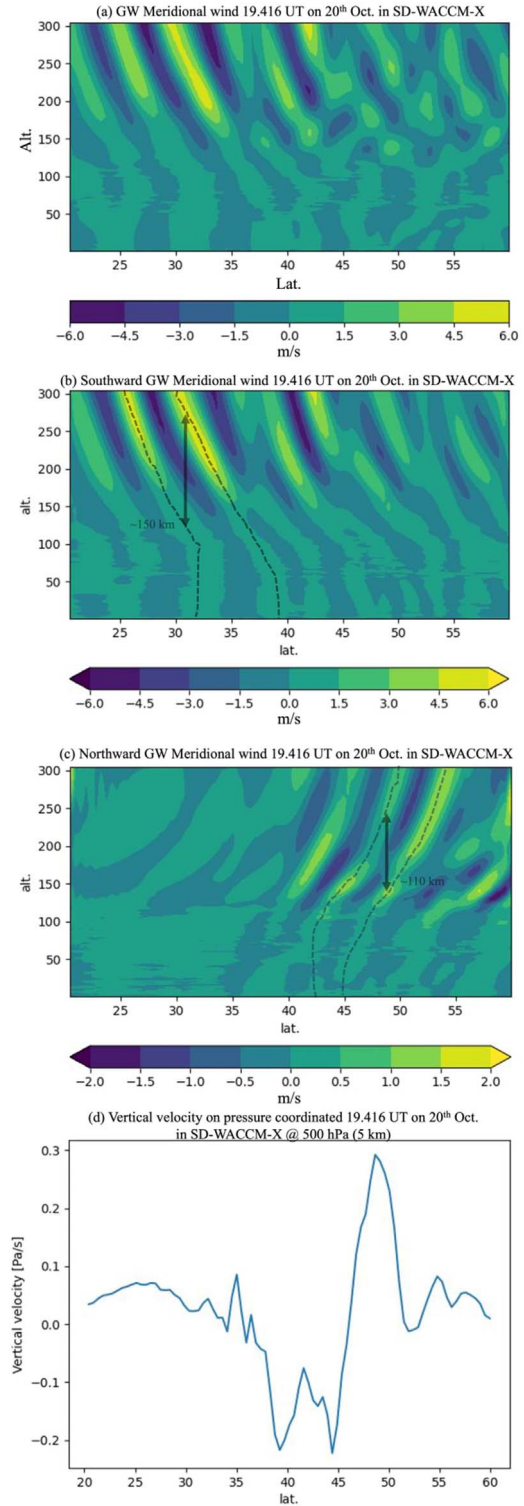

Figure 3. (a) Latitude-vertical cross-section of the GW meridional wind perturbation along 95°W from the surface to 300 km at the same time as in Figures 1 and 2. (b, c) Same as (a) but for the southward and northward propagating GW perturbations, respectively. (d) Vertical velocity at 500 hPa (~5 km) in pressure coordinates (Pa/s) along 95°W at the same time as (a–c). See Movie 2 of the GW meridional winds along 95°W at 16.33–22.33 UT for supporting information.
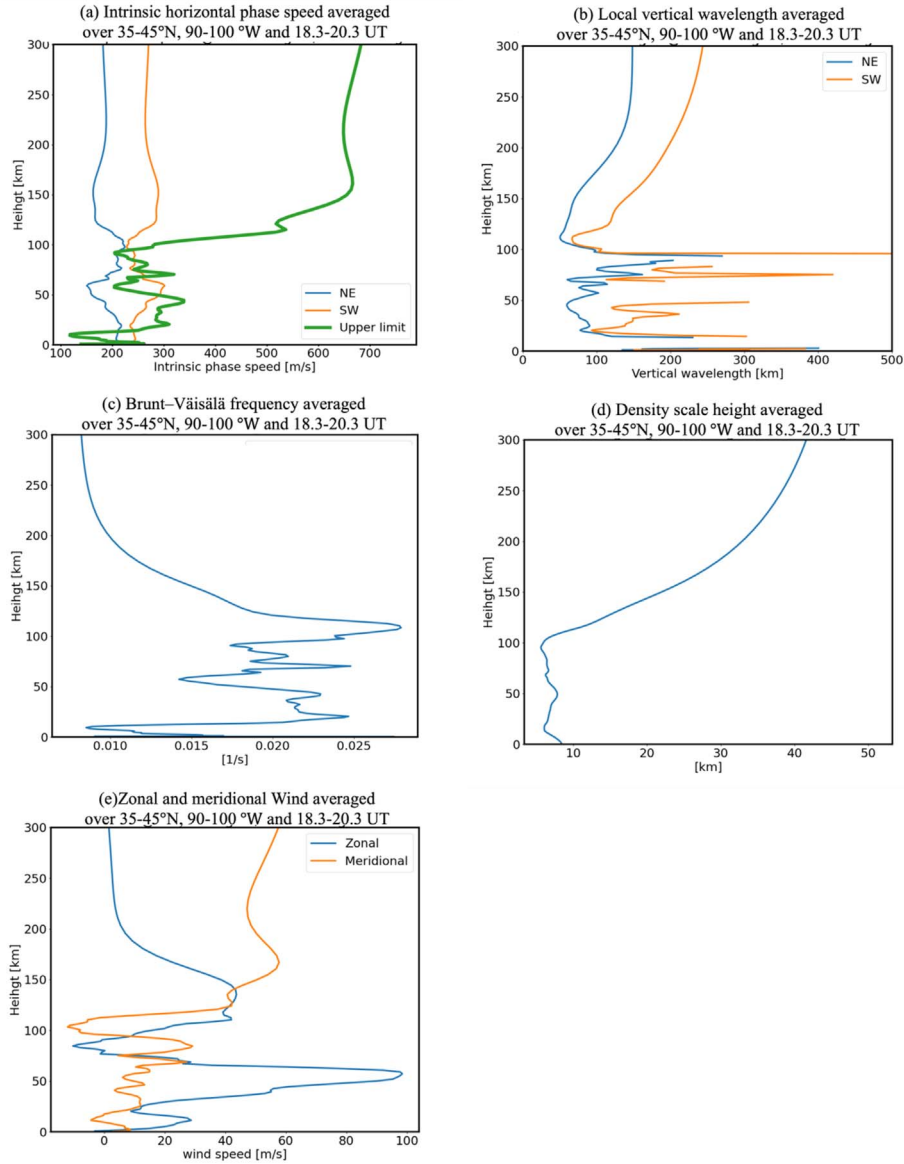
Figure 4. (a) Vertical profiles of GW intrinsic horizontal phase speeds. The blue and orange lines indicate the northeastward and southwestward GWs, respectively. The thick green line indicates the upper limit of intrinsic horizontal phase speed. (b) Same as (a) but local vertical wavelengths from equation (1). (c) Brunt–Väisälä frequency. (d) Density scale height. (e) Horizontal winds. These values are averaged over 35–45°N, 90–100°W, and 18.3–20.3 UT on 20 October 2020.

$$m^2 = \frac{(k^2 + l^2)(N^2 - \hat{\omega}^2)}{(\hat{\omega}^2 - f^2)} - \frac{1}{4H^2}. \qquad (1)$$

Here k, l, and $\hat{\omega}$ are zonal and meridional wavenumbers, and the intrinsic frequency, respectively. N, H, and f are the Brunt–Väisälä frequency, density scale height, and the Coriolis parameter, respectively. This equation assumes that the background is in hydrostatic balance.

The horizontal wavenumber and ground-based frequency for the GWs in the yellow rectangle in Figure 2c were derived from time-longitude and time-latitude cross-sections of the GW meridional wind from the wave phase fronts (not shown). We obtained the zonal wavenumber, $k = \frac{2\pi}{-890}$ rad·km^{-1}, meridional wavenumber, $l = \frac{2\pi}{-780}$ rad·km^{-1}, and ground-based frequency, $\omega = \frac{2\pi}{42}$ rad·min^{-1}. The direction of the wavenumber vector is chosen as southwestward because the southward GWs are dominant over the continental USA (Fig. 3), but we also estimate the vertical wavelength for the northeastward wavenumber vector case. We assume that the wavenumber vector and ground-based frequency are invariant through the propagation; that is, the ground-based phase speed (~230 m·s^{-1}) is also invariant. Figure 4 shows the intrinsic horizontal phase speeds (a), local vertical wavelength from equation (1) (b), Brunt–Väisälä frequency (c), density scale height (d), and horizontal winds (e). These values are averaged over 35–45°N, 90–100°W, and 18.3–20.3 UT. We also calculated an upper limit of internally propagating GW intrinsic horizontal phase speed (C_{hmax}) based on the GW linear theory (a green thick line

in Fig. 4a). When the intrinsic horizontal phase speed is sufficiently smaller than C_{hmax}, a GW is internally propagating and has a real vertical wavenumber; that is, the GW can propagate vertically. Conversely, when the intrinsic horizontal phase speed is close to or larger than C_{hmax}, a GW is evanescent and has an imaginary vertical wavenumber; that is, the GW cannot propagate vertically. The upper limit of the intrinsic phase speed can be approximately described as follows (Vadas & Crowley, 2010; Heale et al., 2022a):

$$C_{hmax} \approx 2NH, \qquad (2)$$

where N and H are the Brunt–Väisälä frequency and density scale height, respectively. This upper limit is derived from equation (1) and corresponds to an infinite vertical wavenumber under the assumption that a horizontal wavelength and the intrinsic frequency are sufficiently larger than $2\pi H$ and f, respectively. The horizontal wavelengths in this event are ~500–700 km, much larger than the density scale height below the lower thermosphere, satisfying the assumption that the horizontal wavelength is much larger than $2\pi H$. Although the intrinsic horizontal phase speed of the southward GWs is less than the upper phase speed limit by ~50 m·s^{-1} in the lower stratosphere, it is larger than the limit at $z \approx$ 40–60 km, denoting that the southward stratospheric GWs are evanescent. The intrinsic phase speed of the northward GWs is larger than the limit in the troposphere. In the thermosphere, the upper phase speed limit drastically increases with altitude, while the GW intrinsic horizontal phase speeds of both southward and northward GWs in Figure 4a are almost the same as those in the altitude range of ~20–100 km, showing that the GWs are freely propagating in the thermosphere. This sharp increase in the upper phase speed limit at $z >$ 100 km is mainly attributed to the increase in the density scale height (Fig. 4d) and the sound speed above ~100 km because the temperature increases dramatically in altitude in the thermosphere. Therefore, this increase in the density scale height could alter the GWs from being evanescent in the middle atmosphere to freely propagating in the thermosphere.

In terms of the vertical wavelengths (Fig. 4b), the local vertical wavelengths averaged in the thermosphere are ~110 km for northward GWs and ~150 km for southward GWs, which is consistent with those in SD-WACCM-X (Fig. 3a). The larger vertical wavelength of the southward GWs is attributed to the strong northward wind (~70 m·s^{-1}) in Figure 4e. The Doppler Effect due to the northward wind increases (decreases) the vertical wavelength of the southward (northward) GWs. Below ~100 km altitude, the local vertical wavelengths were equal to or larger than the thickness of the middle atmosphere (~80 km). In particular, the southward GWs had an infinite (imaginary) vertical wavelength in an altitude range of 50–100 km; in other words, the altitude range of 50–100 km was an evanescent region where the squared GW vertical wavenumber is equal to or smaller than 0 for the southward GWs; thus, the GWs there are evanescent. These large vertical wavelengths are consistent with the vertically constant phases in Figure 3 and the horizontal phase speed in Figure 4a, suggesting that the GWs are evanescent through a large part of the altitude region below ~100 km.

Although evanescent GWs cannot propagate vertically in an evanescent region based on the linear theory, they can transmit their energy through the evanescent region, although the wave amplitude decays with altitude. A meridional wind amplitude of an evanescent GW, $v'_{amp_{(z)}}$, in the Earth's atmosphere can be written based on equation (2.68) in Nappo (2013):

$$v'_{amp_{(z)}} = v'_{amp_{(z_0)}} \exp\left\{ (z - z_0)\left(\frac{1}{2H} - k_z\right) \right\}, \qquad (3)$$

where z, H, k_z, and $v'_{amp_{(z_0)}}$ are altitude, density scale height, the magnitude of the imaginary part of the vertical wavenumber, and amplitude of a GW at z_0, which is the lower boundary of the evanescent layer. This equation assumes the WKB approximation, whereby the background variables slowly vary (Nappo, 2013), and neglects GW dissipation. Equation (3) takes into account the growth of GW amplitude with altitude due to a decrease in the atmospheric density, although Nappo (2013) does not consider it. When the magnitude of an imaginary vertical wavenumber (k_z) is sufficiently less than the inverse of the twice density scale height $\left(\frac{1}{2H}\right)$, evanescent GWs can tunnel through their evanescent region and transmit their energy to higher altitudes (Nappo, 2013; Gavrilov and Kshevetskii, 2018; Inchin et al., 2020; Heale et al., 2022b). The magnitudes of the imaginary vertical wavenumbers calculated from equation (1) between 50 and 100 km range from $\frac{2\pi}{\sim 190}$ to $\frac{2\pi}{\sim 340}$ km^{-1}, which is ~2–4 times smaller than the inverse of two times the density scale height $\left(\frac{1}{\sim 12} \text{ to } \frac{1}{\sim 14} \text{ km}^{-1}\right)$; thus, the southward GWs can tunnel through the middle atmosphere (their evanescent region) into the thermosphere (free propagation altitude). Therefore, the evanescent GWs excited by the convection within the cold front tunnel through the troposphere and the middle atmosphere (~0–100 km), become internally propagating at ~100 km because of the increase in the density scale height, and then propagate to higher altitudes.

3.3 Characteristics of simulated MSTIDs

This sub-section shows MSTIDs caused by the convectively generated GWs in SAMI3/SD-WACCM-X. Figure 5 shows electron density perturbations at 200 km and 300 km altitudes in SAMI3/SD-WACCM-X (Figs. 5a and 5b). Horizontal wavenumbers and propagation directions of the relative (%) electron density perturbations in SAMI3/SD-WACCM-X are similar to those of the GW meridional wind perturbations in Figure 2; that is, both horizontal wavelengths and propagation directions are ~500–700 km and southwestward, respectively. We also found both periods were ~40 min; that is, the TIDs are classified as MSTIDs. The MSTIDs in the simulation have a concentric structure similar to the GWs, although the MSTIDs preferred to propagate southward together with the GWs (see Movie 1 in supporting information). The similar horizontal structures and temporal variability suggest that the MSTIDs were caused by the GWs.

It should be noted that temporal and spatial variations of the simulated MSTIDs were quite different from those of MSTIDs observed by the ground-based Global Navigation Satellite System (GNSS) receivers, although the GNSS observations captured MSTIDs with concentric structures propagating southward from the early season winter storm (see Fig. S1 and Movie 4 in supporting information). Addressing those discrepancies is beyond the focus of this paper.
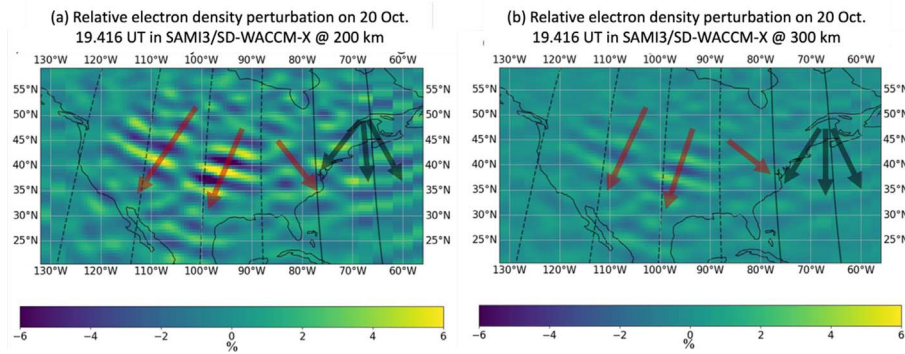
Figure 5. Relative electron density perturbations (%) in SAMI3/SD-WACCM-X at 200 km (a) and 300 km (b).
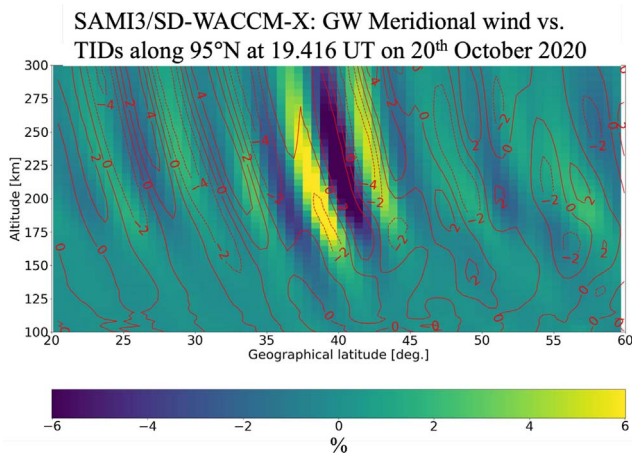

Figure 6. The color plots denote electron density perturbations in SAMI3/SD-WACCM-X (a) along 95°W at 19.416 UT (13.086 LT) on 20th October 2020. The red contours denote the meridional wind perturbations (m·s^{-1}) in SD-WACCM-X.

Figure 6 shows the latitude-vertical cross-section of the electron density perturbations (color plot) with the GW meridional wind perturbation (red contour line) along 95° W at 19.416 UT (13.083 LT) in SAMI3/SD-WACCM-X. It should be noted that the 95° W geographic longitude is almost parallel to the geomagnetic field line. Movie 3 for supporting information shows an animation of Figure 6 from 16.33 to 22.33 UT (10–16 LT). The phases of the perturbations are tilted equatorward with altitude, especially equatorward of ~45°N, suggesting southward and upward propagation. The electron density (~6%) and meridional wind (~4 m·s^{-1}) perturbations display a coherent wave pattern, suggesting these MSTIDs were caused by GWs emitted from convection within the front. The southward preference is attributed to the angle between the GW neutral density perturbations and the magnetic field line (Otsuka et al., 2013). The southward propagating GWs push plasma south-upward to north-downward, while the northward propagating GWs push plasma north-upward to south-downward. The magnetic field line is tilted south-upward to north-downward in the northern hemisphere so that the southward propagating GWs generate MSTIDs more efficiently than the northward propagating ones. Another consequence of the southward preference is that dissipation and filtering by the ambient background winds

preferentially dampen the northward propagating waves, thus contributing to preferential southward MSTID propagation (Crowley et al., 1987; Vadas, 2007). The vertical wavelengths of the GWs with northward propagation are ~110 km, which is smaller than the vertical wavelength of the GWs with southward propagation (~150 km) because of the northward background wind (see Fig. 4e). Thus, it is likely that the dissipation and wind filtering significantly contribute to the southward preference of the MSTIDs, as well.

4 Conclusions

Using SD-WACCM-X and SAMI3/SD-WACCM-X, we simulated GWs and MSTIDs with periods less than 2 h. On 20 October 2020, GWs and MSTIDs propagated together southwestward over the northern-to-eastern central USA We conclude that the GWs generated the MSTIDs. The GWs propagated southwestward with a ~500–700 km horizontal wavelength and ~40 min ground-based period. We identified the following potential sequence of events to explain the simulated GWs and MSTIDs: (1) a cold weather front enhanced upward airflow in the north-central and eastern USA (90–100°N, 38–42°N), and generated evanescent GWs; (2) those evanescent GWs traveled horizontally in all directions but were evanescent in the troposphere and middle atmosphere up to ~100 km altitude. They tunneled through the middle atmosphere because of the large magnitudes of their imaginary vertical wavelengths; (3) those evanescent GWs became internally propagating in the lower thermosphere because of the increase in the sound speed (which is mainly due to the increase of the density scale height), and the GWs propagating southward created the MSTIDs. This favorable southward propagation of the GWs and MSTIDs can be explained by the angle between the propagation direction of the GWs and geomagnetic field lines (Jacobson et al., 1995; Hernández-Pajares et al., 2006; Otsuka et al., 2013) and wind filtering and dissipation due to the Doppler shift (Vadas, 2007).

Previous studies have focused on MSTIDs generated by GWs emitted from tropical cyclones and deep convection during summer, extreme volcanic eruptions, and earthquakes. However, weather fronts are a more common phenomenon in the middle latitudes, and we speculate that convection within fronts is a critically important GW source of concentric MSTIDs. Even though the SD-WACCM-X model resolution is two times higher than in the previous global model study

(Miyoshi et al., 2018), its effective resolution is still too coarse to resolve convection within a weather front. Indeed, it is clear from Figure 2 that the effective horizontal wavelength is ~500 km. To resolve convection, models need kilometer-scale horizontal resolution (Hirt et al., 2019) and high vertical resolution as well (Colbert et al., 2019). In addition, model dynamics need to be non-hydrostatic, and non-hydrostatic model dynamics furthermore need to include suitable parameterizations of unresolved processes by turbulent eddies in the boundary layer (e.g., parameterization of convective initiation) (Hirt et al., 2019; Ishida et al., 2022). Because convectively generated GW spectra depend on a cumulus parameterization scheme and finer resolution models reproduce GW spectra more accurately (Lane & Knievel, 2005; Kim et al., 2009), convectively generated GWs are more robust in the real atmosphere than in SD-WACCM-X.

Supplementary material

The supplementary material of this article is available at https://www.swsc-journal.org/10.1051/swsc/2024036/olm.

Figure S1: (a) Total electron density content (TEC) perturbations in GNSS at 21.258 UT on 20 October 2020. The perturbations were derived in accordance with Chou et al. (2023), but a Butterworth filter with 10–60-min cutoff period was applied in this paper. The perturbations were averaged over 0.47° × 0.625° bins to align with the grid of the SD-WACCM-X output. (b) The same as (a), but in SAMI3/SD-WACCM-X. The black dashed lines in (a) and (b) denote the crests of concentric waves. (c) Radar reflectivity in NEXRAD. The red box indicates convection in the cold front area; i.e., the high convective activity area.

Movie 1: Gravity wave meridional wind perturbations $(m \cdot s^{-1})$ at 50 km (a), 100 km (b), 200 km (c), and 300 km (d) altitudes at 16.33 and 22.33 UT on 20 October in SD-WACCM-X.

Movie 2: (a) Latitude-vertical cross-section of the GW meridional wind perturbation along 95 W from the surface to 300 km at 16.33–22.33 UT. (b, c) Same as (a) but for the southward and northward propagating GW perturbations, respectively.

Movie 3: The color plots denote electron density perturbations in SAMI3/SD-WACCM-X (a) along 95 W at 16.33–22.33 UT on 20th October 2020. The red contours denote the meridional wind perturbations $(m \cdot s^{-1})$ in SD-WACCM-X.

Movie 4: Total electron density content (TEC) perturbations in GNSS at 16.33–22.33 on 20 October 2020. The perturbations were derived in accordance with Chou et al. (2023), but a Butterworth filter with 10–60-minute cutoff period was applied

in this paper. The perturbations were averaged over bins to align with the grid of the SD-WACCM-X output. (b) The same as (a), but in SAMI3/SD-WACCM-X.

References

Azeem I, Yue J, Hoffmann L, Miller SD, Straka III WC, Crowley G. 2015. Multisensor profiling of a concentric gravity wave event propagating from the troposphere to the ionosphere. *Geophys Res Lett* **42**: 7874–7880. https://doi.org/10.1002/2015GL065903.

Azeem I, Vadas SL, Crowley G, Makela JJ. 2017. Traveling ionospheric disturbances over the United States induced by gravity waves from the 2011 Tohoku tsunami and comparison with gravity wave dissipative theory. *J Geophys Res Space Phys* **122**: 3430–3447. https://doi.org/10.1002/2016JA023659.

Boška J, Šauli P. 2001. Observations of gravity waves of meteorological origin in the F-region ionosphere. *Phys Chem Earth Part C Solar Terrest Planet Sci* **26(6)**: 425–428. https://doi.org/10.1016/S1464-1917(01)00024-1.

Chou MY, Lin CCH, Yue J, Tsai HF, Sun YY, Liu JY, Chen CH. 2016. Concentric traveling ionosphere disturbances triggered by Super Typhoon Meranti. *Geophys Res Lett* **44**: 1219–1226. https://doi.org/10.1002/2016GL072205.

Chou M-Y, Yue J, Lin CCH, Rajesh PK, Pedatella NM. 2022. Conjugate effect of the 2011 Tohoku reflected tsunami-driven gravity waves in the ionosphere. *Geophys Res Lett* **49**: e2021GL097170. https://doi.org/10.1029/2021GL097170.

Chou M-Y, Yue J, Sassi F, McDonald S, Tate J, et al. 2023. Modeling the day-to-day variability of midnight equatorial plasma bubbles with SAMI3/SD-WACCM-X. *J Geophys Res Space Phys* **128**: e2023JA031585. https://doi.org/10.1029/2023JA031585.

Crowley G, Jones TB, Dudeney JR. 1987. Comparison of short period TID morphologies in Antarctica during geomagnetically quiet and active intervals. *J Atmos Terrest Phys* **49**(**11–12**): 1155–1162. https://doi.org/10.1016/0021-9169(87)90098-5.

Crowley G, Rodrigues FS. 2012. Characteristics of traveling ionospheric disturbances observed by the TIDDBIT sounder. *Radio Sci* **47(4)**: 1–12. https://doi.org/10.1029/2011RS004959.

Colbert M, Stensrud DJ, Markowski PM, Richardson YP. 2019. Processes associated with convection initiation in the North American Mesoscale Forecast System, version 3 (NAMv3). *Weather Forecast* **34**: 683–700. https://doi.org/10.1175/WAF-D-18-0175.1.

Fritts DC, Vadas SL. 2008. Gravity wave penetration into the thermosphere: sensitivity to solar cycle variations and mean winds. *Ann Geophys* **26**: 3841–3861. https://doi.org/10.5194/angeo-26-3841-2008.

Gavrilov NM, Kshevetskii SP. 2018. Features of the supersonic gravity wave penetration from the Earth's surface to the upper atmosphere. *Radiophys Quantum Electron* **61**: 243–252. https://doi.org/10.1007/s11141-018-9885-4.

Gelaro R, McCarty W, Suárez JM, Todling R, Molod A, et al. 2017. The modern-era retrospective analysis for research and applications, version 2 (MERRA-2). *J Clim* **30**: 5419–5454. https://doi.org/10.1175/JCLI-D-16-0758.1.

Heale CJ, Lund T, Fritts DC. 2020. Convectively generated gravity waves during solstice and equinox conditions. *J Geophys Res Atmos* **125**: e2019JD031582. https://doi.org/10.1029/2019JD031582.

Heale CJ, Inchin PA, Snively JB. 2022. Primary versus secondary gravity wave responses at F-region heights generated by a convective source. *J Geophys Res Space Phys* **127**: e2021JA029947. https://doi.org/10.1029/2021JA029947.

Heale CJ, Bossert K, Vadas SL. 2022. 3D numerical simulation of secondary wave generation from mountain wave breaking over

Europe. *J Geophys Res Atmos* **127**: e2021JD035413. https://doi.org/10.1029/2021JD035413.

Hernández-Pajares M, Juan JM, Sanz J. 2006. Medium-scale traveling ionospheric disturbances affecting GPS measurements: spatial and temporal analysis. *J Geophys Res* **111**: A07S11. https://doi.org/10.1029/2005JA011474.

Hernández-Pajares M, Garcia-Fernàndez M, Rius A, Notarpietro R, von Engeln A, Olivares-Pulido G, Aragón-Àngel À, García-Rigo A. 2017. Electron density extrapolation above F2 peak by the linear Vary-Chap model supporting new Global Navigation Satellite Systems-LEO occultation missions. *J Geophys Res Space Phys* **122**: 9003–9014. https://doi.org/10.1002/2017JA023876.

Hines CO. 1960. Internal atmospheric gravity waves at ionospheric heights. *Can J Phys* **38(11)**: 1441–1481. https://doi.org/10.1139/p60-150.

Hirt M, Rasp S, Blahak U, Craig GC. 2019. Stochastic parameter-ization of processes leading to convective initiation in kilometer-scale models. *Month Weather Rev* **147**: 3917–3934. https://doi.org/10.1175/MWR-D-19-0060.1.

Hocke K, Schlegel K. 1996. A review of atmospheric gravity waves and travelling ionospheric disturbances: 1982–1995. *Ann Geophys* **14**: 917–940. https://doi.org/10.1007/s00585-996-0917-6.

Holton JR, Hakim GJ. 2013. An introduction to dynamic meteorol-ogy, Academic press, ISBN:0123848660.

Hoffmann L, Xue X, Alexander MJ. 2013. A global view of stratospheric gravity wave hotspots located with atmospheric infrared sounder observations. *J Geophys Res Atmos* **118**: 416–434. https://doi.org/10.1029/2012JD018658.

Huba JD, Joyce G, Krall J. 2008. Three-dimensional equatorial spread *F* modeling. *Geophys Res Lett* **35**: L10102. https://doi.org/10.1029/2008GL033509.

Huba JD, Joyce G, Fedder JA. 2000. Sami2 is Another Model of the Ionosphere (SAMI2): a new low-latitude ionosphere model. *J Geophys Res* **105(A10)**: 23035–23053. https://doi.org/10.1029/2000JA000035.

Huba JD, Drob DP, Wu T-W, Makela JJ. 2015. Modeling the ionospheric impact of tsunami-driven gravity waves with SAMI3: conjugate effects. *Geophys Res Lett* **42**: 5719–5726. https://doi.org/10.1002/2015GL064871.

Huba JD, Maute A, Crowley G. 2017. SAMI3_ICON: model of the ionosphere/plasmasphere system. *Space Sci Rev* **212**: 731. https://doi.org/10.1007/s11214-017-0415-z.

Huba JD, Krall J. 2013. Impact of meridional winds on equatorial spread F: revisited. *Geophys Res Lett* **40**: 1268–1272. https://doi.org/10.1002/grl.50292.

Huba JD, Liu H-L. 2020. Global modeling of equatorial spread F with SAMI3/WACCM-X. *Geophys Res Lett* **47**: e2020GL088258. https://doi.org/10.1029/2020GL088258.

Hung RJ, Kuo JP. 1978. Ionospheric observation of gravity-waves associated with Hurricane Eloise. *J Geophys* **45**: 67–80. https://n2t.net/ark:/88439/y031553.

Hunsucker RD. 1982. Atmospheric gravity waves generated in the high-latitude ionosphere: a review. *Rev Geophys* **20(2)**: 293–315. https://doi.org/10.1029/RG020i002p00293.

Jacobson AR, Carlos RC, Massey RS, Wu G. 1995. Observations of traveling ionospheric disturbances with a satellite-beacon radio interferometer: seasonal and local time behavior. *J Geophys Res* **100(A2)**: 1653–1665. https://doi.org/10.1029/94JA02663.

Inchin PA, Heale CJ, Snively JB, Zettergren MD. 2020. The dynam-ics of nonlinear atmospheric acoustic-gravity waves generated by tsunamis over realistic bathymetry. *J Geophys Res Space Phys* **125**: e2020JA028309. https://doi.org/10.1029/2020JA028309.

Ishida J, Aranami K, Kawano K, Matsubayashi K, Kitamura Y, Muroi C. 2022. ASUCA: the JMA operational non-hydrostatic model. *J Meteorol Soc Japan* **100**: 825–846. https://doi.org/10.2151/jmsj.2022-043.

Kelley MC, Miller CA. 1997. Electrodynamics of midlatitude spread F, 3. Electrohydrodynamic waves? A new look at the role of electric fields in thermospheric wave dynamics. *J Geophys Res* **102**: 11539–11547. https://doi.org/10.1029/96JA03841.

Kim S-Y, Chun H-Y, Wu D. 2009. A study on stratospheric gravity waves generated by Typhoon Ewiniar: numerical simulations and satellite observations. *J Geophys Res* **114**: D22104. https://doi.org/10.1029/2009JD011971.

Kotake N, Otsuka Y, Ogawa T, Tsugawa T, Saito A. 2007. Statistical study of medium-scale traveling ionospheric disturbances observed with the GPS networks in Southern California. *Earth Planet Space* **59**: 95–102. https://doi.org/10.1186/BF03352681.

Lane TP, Knievel JC. 2005. Some effects of model resolution on simulated gravity waves generated by deep, mesoscale convection. *J Atmos Sci* **62**: 3408–3419. https://doi.org/10.1175/JAS3513.1.

Lee WK, Kil H, Paxton LJ. 2021. Global distribution of nighttime MSTIDs and its association with E region irregularities seen by CHAMP satellite. *J Geophys Res Space Phys* **126**: e2020JA028836. https://doi.org/10.1029/2020JA028836.

Liu H-L, McInerney JM, Santos S, Lauritzen PH, Taylor MA, Pedatella NM. 2014. Gravity waves simulated by high-resolution whole atmosphere community climate model. *Geophys Res Lett* **41**: 9106–9112. https://doi.org/10.1002/2014GL062468.

Liu JY, Chen CH, Lin CH, Tsai HF, Chen CH, Kamogawa M. 2011. Ionospheric disturbances triggered by the 11 March 2011 M9.0 Tohoku earthquake. *J Geophys Res* **116**: A06319. https://doi.org/10.1029/2011JA016761.

Liu H-L, Bardeen CG, Foster BT, Lauritzen P, Liu J, Lu G, et al. 2018. Development and validation of the Whole Atmosphere Community Climate Model with thermosphere and ionosphere extension (WACCM-X 2.0). *J Adv Model Earth Syst* **10**: 381–402. https://doi.org/10.1002/2017MS001232.

Marks CJ, Eckermann SD. 1995. A three-dimensional nonhydrostatic ray-tracing model for gravity waves: formulation and preliminary results for the middle atmosphere. *J Atmos Sci* **52(11)**: 1959–1984. https://doi.org/10.1175/1520-0469(1995)052<1959:ATDNRT>2.0.CO;2.

Martinis C, Baumgardner J, Wroten J, Mendillo M. 2011. All-sky imaging observations of conjugate medium-scale traveling iono-spheric disturbances in the American sector. *J Geophys Res* **116**: A05326. https://doi.org/10.1029/2010JA016264.

McDonald SE, Sassi F, Mannucci AJ. 2015. SAMI3/SD-WACCM-X simulations of ionospheric variability during northern winter 2009. *Space Weather* **13**: 568–584. https://doi.org/10.1002/2015SW001223.

McDonald SE, Sassi F, Tate J, McCormack J, Kuhl DD, Drob DP, Metzler C, Mannucci AJ. 2018. Impact of non-migrating tides on the low latitude ionosphere during a sudden stratospheric warming event in January 2010. *J Atmos Solar Terrest Phys* **171**: 188–200. https://doi.org/10.1016/j.jastp.2017.09.012.

Miller CA, Swartz WE, Kelley MC, Mendillo M, Nottingham D, Scali J, Reinisch B. 1997. Electrodynamics of midlatitude spread F: 1. Observations of unstable, gravity wave-induced ionospheric electric fields at tropical latitudes. *J Geophys Res* **102(A6)**: 11521–11532. https://doi.org/10.1029/96JA03839.

Miyoshi Y, Jin H, Fujiwara H, Shinagawa H. 2018. Numerical study of traveling ionospheric disturbances generated by an upward propagating gravity wave. *J Geophys Res Space Phys* **123**: 2141–2155. https://doi.org/10.1002/2017JA025110.

Nappo CJ. 2013. An introduction to atmospheric gravity waves. Academic Press. ISBN: 978-0-12-385223-6.

Nicolls MJ, Vadas SL, Aponte N, Sulzer MP. 2014. Horizontal parameters of daytime thermospheric gravity waves and E region neutral winds over Puerto Rico. *J Geophys Res Space Phys* **119**: 575–600. https://doi.org/10.1002/2013JA018988.

Nishioka M, Tsugawa T, Kubota M, Ishii M. 2013. Concentric waves and short-period oscillations observed in the ionosphere after the 2013 Moore EF5 tornado. *Geophys Res Lett* **40**: 5581–5586. https://doi.org/10.1002/2013GL057963.

Otsuka Y. 2021. Medium-scale traveling ionospheric disturbances. In: *Ionosphere dynamics and applications, geophysical monograph series*, pp. 421–437 (eds C. Huang, G. Lu, Y. Zhang, L.J. Paxton). https://doi.org/10.1002/9781119815617.ch18.

Otsuka Y, Suzuki K, Nakagawa S, Nishioka M, Shiokawa K, Tsugawa T. 2013. GPS observations of medium-scale traveling ionospheric disturbances over Europe. *Ann Geophys* **31**: 163–172. https://doi.org/10.5194/angeo-31-163-2013.

Perwitasari S, Nakamura T, Tsugawa T, Nishioka M, Tomikawa Y, Ejiri MK, et al. 2022. Propagation direction analyses of medium-scale traveling ionospheric disturbances observed over North America with GPS-TEC perturbation maps by three-dimensional spectral analysis method. *J Geophys Res Space Phys* **127**: e2020JA028791. https://doi.org/10.1029/2020JA028791.

Perkins F. 1973. Spread F and ionospheric currents. *J Geophys Res* **78**: 218–226. https://doi.org/10.1029/JA078i001p00218.

Pedatella NM, Liu H-L, Marsh DR, Raeder K, Anderson JL. 2019. Error growth in the mesosphere and lower thermosphere based on hindcast experiments in a whole atmosphere model. *Space Weather* **17**: 1442–1460. https://doi.org/10.1029/2019SW002221.

Plougonven R, Zhang F. 2014. Internal gravity waves from atmospheric jets and fronts. *Rev Geophys* **52**: 33–76. https://doi.org/10.1002/2012RG000419.

Sassi F, Liu H-L, Ma J, Garcia RR. 2013. The lower thermosphere during the northern hemisphere winter of 2009: a modeling study using high-altitude data assimilation products in WACCM-X. *J Geophys Res* **118**: 8954–8968. https://doi.org/10.1002/jgrd.50632.

Shiokawa K, Otsuka Y, Ihara C, Ogawa T, Rich FJ. 2003. Ground and satellite observations of nighttime medium-scale traveling ionospheric disturbance at midlatitude. *J Geophys Res* **108(A4)**: 1145. https://doi.org/10.1029/2002JA009639.

Smith AK, Pedatella NM, Marsh DR, Matsuo T. 2017. On the dynamical control of the mesosphere-lower thermosphere by the lower and middle atmosphere. *J Atmos Sci* **74(3)**: 933–947. https://doi.org/10.1175/JAS-D-16-0226.1.

Stewart RE, Bachand D, Dunkley RR, Giles AC, Lawson B, Legal L, Miller ST, Yau MK. 1995. Winter storms over Canada. *Atmos Ocean* **33(2)**: 223–247. https://doi.org/10.1080/07055900.1995.9649533.

Stull RB. 1976. Internal gravity waves generated by penetrative convection. *J Atmos Sci* **33**: 1279–1286. https://doi.org/10.1175/1520-0469(1976)033<1279:IGWGBP>2.0.CO;2.

Taylor MJ, Hapgood MA. 1988. Identification of a thunderstorm as a source of short period gravity waves in the upper atmospheric nightglow emissions. *Planet Space Sci* **36**: 975–985. https://doi.org/10.1016/0032-0633(88)90035-9.

Takahashi H, Figueiredo CAOB, Essien P, Wrasse CM, Barros D, Nyassor PK, Paulino I, Egito F, Rosa GM, Sampaio AHR. 2022. Signature of gravity wave propagations from the troposphere to ionosphere. *Ann Geophys* **40**: 665–672. https://doi.org/10.5194/angeo-40-665-2022.

Tapp MC, White PW. 1976. A non-hydrostatic mesoscale model. *Quart J Royal Meteorol Soc* **102**: 277–296. https://doi.org/10.1002/qj.49710243202.

Themens DR, Watson C, Žagar N, Vasylkevych S, Elvidge S, McCaffrey A, et al. 2022. Global propagation of ionospheric disturbances associated with the 2022 Tonga volcanic eruption. *Geophys Res Lett* **49**: e2022GL098158. https://doi.org/10.1029/2022GL098158.

Vadas SL. 2007. Horizontal and vertical propagation and dissipation of gravity waves in the thermosphere from lower atmospheric and thermospheric sources. *J Geophys Res* **112**: A06305. https://doi.org/10.1029/2006JA011845.

Vadas SL. 2013. Compressible f-plane solutions to body forces, heatings, and coolings, and application to the primary and secondary gravity waves generated by a deep convective plume. *J Geophys Res Space Phys* **118**: 2377–2397. https://doi.org/10.1002/jgra.50163.

Vadas SL, Fritts DC. 2004. Thermospheric responses to gravity waves arising from mesoscale convective complexes. *J Atmos Solar Terrest Phys* **66(6–9)**: 781–804. https://doi.org/10.1016/j.jastp.2004.01.025.

Vadas SL, Fritts DC. 2009. Reconstruction of the gravity wave field from convective plumes via ray tracing. *Ann Geophys* **27**: 147–177. https://doi.org/10.5194/angeo-27-147-2009.

Vadas SL, Liu H. 2009. Generation of large-scale gravity waves and neutral winds in the thermosphere from the dissipation of convectively generated gravity waves. *J Geophys Res* **114**: A10310. https://doi.org/10.1029/2009JA014108.

Vadas SL, Liu H-L. 2013. Numerical modeling of the large-scale neutral and plasma responses to the body forces created by the dissipation of gravity waves from 6 h of deep convection in Brazil. *J Geophys Res Space Phys* **118**: 2593–2617. https://doi.org/10.1002/jgra.50249.

Vadas SL, Crowley G. 2010. Sources of the traveling ionospheric disturbances observed by the ionospheric TIDDBIT sounder near Wallops Island on 30 October 2007. *J Geophys Res* **115**: A07324. https://doi.org/10.1029/2009JA015053.

Vadas SL, Jia Y, Joe S, Pete S, Alan L. 2009. A model study of the effects of winds on concentric rings of gravity waves from a convective plume near Fort Collins on 11 May 2004. *J Geophys Res* **114**: D06103. https://doi.org/10.1029/2008JD010753.

Vadas SL, Azeem I. 2021. Concentric secondary gravity waves in the thermosphere and ionosphere over the continental United States on March 25–26, 2015 from deep Convection. *J Geophys Res Space Phys* **126**: e2020JA028275. https://doi.org/10.1029/2020JA028275.

Vadas SL, Figueiredo C, Becker E, Huba JD, Themens DR, Hindley N, Mrak S, Galkin I, Bossert K. 2023. Traveling ionospheric disturbances induced by the secondary gravity waves from the Tonga eruption on 15 January 2022: modeling with MESORAC-HIAMCM-SAMI3 and comparison with GPS/TEC and ionosonde data. *J Geophys Res Space Phys* **128(6)**: e2023JA031408. https://doi.org/10.1029/2023JA031408.

Walterscheid RL, Hecht JH. 2003. A reexamination of evanescent acoustic-gravity waves: special properties and aeronomical significance. *J Geophys Res* **108(D11)**: 4340. https://doi.org/10.1029/2002JD002421.

Wright CJ, Hindley NP, Alexander MJ, Barlow M, Hoffmann L, et al. 2022. Surface-to-space atmospheric waves from Hunga Tonga–Hunga Ha'apai eruption. *Nature* **609**: 741–746. https://doi.org/10.1038/s41586-022-05012-5.

Xu S, Vadas SL, Yue J. 2024. Quiet time thermospheric gravity waves observed by GOCE and CHAMP. *J Geophys Res Space Phys* **129**: e2023JA032078. https://doi.org/10.1029/2023JA032078.

Yang Z, Gu S-Y, Qin Y, Teng C-K, Huang F, Sun W, Dou X. 2022. Statistical study of F-region short period ionospheric disturbances related to convection in the lower atmosphere over Wuhan, China. *Space Weather* **20**: e2022SW003140. https://doi.org/10.1029/2022SW003140.

Yokoyama T, Hysell DL. 2010. A new midlatitude ionosphere electrodynamics coupling model (MIECO): latitudinal dependence and propagation of medium-scale traveling ionospheric disturbances. *Geophys Res Lett* **37**: L08105. https://doi.org/10.1029/2010GL042598.

Zawdie K, Belehaki A, Burleigh M, Chou M-Y, Dhadly MS. 2022. Impacts of acoustic and gravity waves on the ionosphere. *Front Astron Space Sci* **9**: 1064152. https://doi.org/10.3389/fspas.2022.1064152.

Zettergren MD, Snively JB. 2015. Ionospheric response to infrasonic-acoustic waves generated by natural hazard events. *J Geophys Res Space Phys* **120**: 8002–8024. https://doi.org/10.1002/2015JA021116.

Zhang S-R, Vierinen J, Ercha A, Goncharenko LP, Philip JE, William R, Anthea JC, Andre S. 2022. Tonga volcanic eruption induced global propagation of ionospheric disturbances via lamb waves. *Front Astron Space Sci* **9**: 871275. https://www.frontiersin.org/articles/10.3389/fspas.2022.871275.